

Interfacial Engineering Strategy to Avoid Oxidation Reaction and Boost Charge Transport Kinetics of Microparticle Silicon Larger than 5 μm for Stable Full Cell Lithium-Ion Battery

Junhyuk Ji, Junchae Jeong, Seochan Hong, Yongju Lee, Donghyuk Kim, and Won Bae Kim*

Demand for advanced energy storage technologies has spurred interest in lithium-ion batteries (LIBs) with silicon (Si) anodes promising higher energy-density due to superior theoretical capacity. However, Si anodes face challenges such as significant volumetric expansion, low electrical conductivity, and safety concerns due to gas evolution. This study addresses these issues by introducing nitrogen-doped hard carbon (NHC) layer onto microparticle silicon (mSi, $\approx 5 \mu\text{m}$) using scalable wet-chemical coating technique followed by optimal carbonization. The NHC layer successfully suppresses hydrogen (H_2) gas evolution by effectively passivating interface to deactivate oxidation reaction. Electrochemical evaluations demonstrate that the NHC layer induces effective solid electrolyte interphase, improves lithium-

ion (Li^+) diffusion kinetics, and mitigates volumetric expansion of mSi anodes, thereby reducing electrolyte decomposition and enhancing cycling stability. In practical coin-type full cell systems, mSi@NHC-700-20 cell paired with $\text{LiNi}_{0.65}\text{Co}_{0.15}\text{Mn}_{0.20}\text{O}_2$ cathode exhibits superior areal capacities over 0.85 and 0.84 mAh cm^{-2} after 300 cycles at 1 C/0.5 C and 3 C/3 C charge/discharge rates, with ultrastable capacity retention at decay rates of 0.24 % and 0.22 %, respectively. This scalable coating strategy effectively bridges the gap between laboratory-scale research and industrial applications, positioning mSi@NHC anode as a highly promising solution for high-energy-density LIBs in advanced energy storage systems.

1. Introduction

With gradually intensified demands on advanced energy storage technologies that play a significant role in our modern life, global attentions have mainly focused on lithium-ion batteries (LIBs) driven by their versatile applications and sustainable clean energy technologies.^[1–5] Despite the fact that global electric vehicle sales surged in 2022, effectively taking over the battery market compared to 2021, the increase in energy density of commercial batteries remains notably sluggish; from the first generation of lead-acid cells ($\approx 40 \text{ Wh kg}^{-1}$) to current LIBs ($\approx 240 \text{ Wh kg}^{-1}$),

the practical energy density has only increased sixfold.^[6,7] Given the increasing need for higher energy density in advanced battery systems, silicon (Si) materials have emerged as a potential solution to replace graphite anodes due to their superior theoretical capacity (3579 mAh g^{-1} for $\text{Li}_{15}\text{Si}_4$) and suitable working voltage ($< 0.4 \text{ V}$ vs. Li/Li^+).^[8] Nonetheless, Si anodes are experiencing several technological challenges. At first, they face large volumetric expansion ($> 300 \%$) during their electrochemical lithium alloying reaction, severely compromising structural integrity and leading to Si pulverization and early cycle failure.^[9] Second, low electrical conductivity ($2.52 \times 10^{-6} \text{ S cm}^{-1}$) hinders the destroyed Si particles to participate in subsequent cycling owing to loss of electrical contact between active materials and electrode framework.^[10] Third, Si electrodes show considerable Li^+ concentration gradients inducing incomplete ion extraction and crack generation during lithiation/delithiation process due to low Li^+ diffusion kinetics.^[11,12] Moreover, H_2 gas evolution from oxidation of Si particles in aqueous slurry state tends to be neglected when working at laboratory scale which could induce serious safety issue.^[13,14] As a result, numerous studies have addressed aforementioned problems through nanoscale engineering including nanoparticles, nanopores, nanotubes, and hollow structures to improve structural stability, boost Li^+ kinetics, and thereby enhance capacity retention.^[15,16] Regardless of electrochemical enhancements for nanoscale Si in laboratory, the solutions are hard to fulfill market standard due to complex synthetic management with poor scalability, low tap density, and side reactions. Therefore, various works have subsequently turned their interests into microparticle Si (mSi) anode as a

J. Ji, W. B. Kim

Department of Chemical Engineering
Pohang University of Science and Technology (POSTECH)
77 Cheongam-ro, Nam-gu, Pohang-si, Gyeongsangbuk-do 37673, Republic of Korea

E-mail: kimwb@postech.ac.kr

J. Jeong, S. Hong, W. B. Kim

Department of Battery Engineering
Graduate Institute of Ferrous and Eco Materials Technology (GIFT)
Pohang University of Science and Technology (POSTECH)
77 Cheongam-ro, Nam-gu, Pohang-si, Gyeongsangbuk-do 37673, Republic of Korea

Y. Lee, D. Kim

Battery R&D Campus
LG Energy Solution (LGES), Ltd.
Research Park
188 Munji-ro, Yuseong-gu, Daejeon 34122, Republic of Korea



Supporting information for this article is available on the WWW under <https://doi.org/10.1002/batt.202500037>

promising choice to meet industrial utilization by reducing manufacturing costs of advanced battery systems.^[17]

To diminish a gap between lab-scale research and industrial requirement, we have employed a market-demanded mSi ($\approx 5 \mu\text{m}$), which is larger than previously studied anode particle in size of $1\text{--}2 \mu\text{m}$, demonstrating significant benefits such as a smaller specific surface area, higher volumetric capacity, larger tap density, and lower synthesis cost.^[15,17,18] However, the development of a large-sized mSi anode could surpass their yield and ultimate strengths, resulting in particle fracture and electrode delamination with newly formed Si surface, and the exposed fragments show undesirable and high reactivity, which provokes cell failure and safety issues through continuous decomposition of electrolyte, developing unstable and excessive solid-electrolyte interphase (SEI) layer.^[19,20] Therefore, to deliberate those inevitable challenges, various strategies have been explored such as structure modulation, formation of composite with metal or organic/inorganic chemicals, multifunctional binder, and novel electrolyte design.^[21–23] Among a number of methods, integration of commercially available mSi with a carbon matrix has recently recognized as a crucial surface modification technique to deliver a stable LIB system.^[21,24] The carbon coating layer on Si materials, widely known as a Si/C system, affords excellent cycling stability with cost-effectiveness, attributed to enhanced flexibility, conductivity, and mechanical strength by acting as a buffering space for considerable volume change of Si and as an electrical conducting pathway during lithiation/delithiation process.^[25] Additionally, it has been demonstrated that doping amorphous carbon with heterogeneous elements, such as nitrogen, imparts several properties: (1) generated numerous defects and doped elements during carbonization acting as active sites for Li^+ storage; (2) increased layer spacing facilitating rapid Li^+ diffusion; and (3) improved structural stability and conductivity.^[26] Hence, the surface modification with N-doped carbon layer can preserve the integrity and enhance the Li^+ mobility of mSi anodes, thereby boosting electrochemical kinetics.

However, Si/C composites reported in several studies have still faced challenges such as complicated preparation-synthesis processes, costly equipment, hazardous chemical use, and long-time conventional procedures, which are detrimental to their industrial development for high-energy-density Si anodes despite prolonged cycling lifespan.^[26] Besides, most approaches are centered on enhancing cell performance, and they usually do not address the issue of gas generation, which can cause significant problems like explosions in commercial mass production lines.^[13,14,27] Even more, most methods for the carbon coating attempt synthesis with Si particles on a milligram scale, which should verify their suitability for large-scale production at an industrial level. Therefore, the development of simple and scalable methods with industrial applicability is crucial for advanced mSi anodes in LIBs.

Herein, we present a highly conductive, chemically stable, and mechanically robust N-doped hard carbon (NHC) layer that is chemically integrated on the mSi surface through direct assembly by in situ self-polymerization reaction of dopamine with/without subsequent carbonization process (mSi@x-y),

demonstrating affordable procedure utilizing a wet chemical process with industrially available large-sized Si ($\approx 5 \mu\text{m}$) and accessible nitrogen-carbon sources of polydopamine (PDA), for the effective anode of advanced rechargeable LIBs. As the fabrication process was developed on a multi-gram scale basis, it suggested feasibility for scaling up to larger systems capable of mixing mSi and dopamine monomer. This uniform heteroatom-doped conductive carbon layer could effectively passivate the active interface between mSi and electrolyte, successfully suppressing mainly evolved H_2 gas from aqueous slurry by restraining oxidation reaction on mSi surface to handle very important industrial safety issue. Moreover, the NHC provided the accelerated Li^+ diffusive pathways and numerous active sites for enhanced ionic/electronic conductivity and Li^+ capacitive contribution. In addition, the integrated layer provided solid physical support to withstand volumetric expansion of mSi during repeated lithiation/delithiation by dissipating considerable stress, thereby enhancing structural stability at both the particle and electrode levels to reduce undesirable electrolyte decomposition on the newly generated Si surface and forming robust SEI layer with enriched lithium fluoride (LiF) and lithium carbonate (Li_2CO_3) even at high current density condition (Figure 1). From a practical perspective using coin-type full cell systems pairing with NCM651520 (Ni65) cathode, the rationally designed conductive NHC-applied protective layer on mSi surface achieved remarkable cyclic stability with superior areal capacity of over 0.85 mAh cm^{-2} and 0.84 mAh cm^{-2} even after 300 cycles (i) at a practical harsh condition of 1 C charge/0.5 C discharge and (ii) even at a fast condition of 3 C charge/3 C discharge demonstrating only 0.24 % and 0.22 % capacity decay rate, respectively. This commercial-level accepted surface modification design with multifunctional conductive carbon strategy could suggest a practical potential to promote the mSi-based LIB anodes as outperforming energy storage materials.

2. Results and Discussion

2.1. Preparation and Characterization of the N-doped Carbon-Coated mSi

The polymeric PDA layer on the mSi surface was directly fabricated without any notable morphological deviation (Figure S1a, b, Supporting Information) by a feasible, direct oxidative in situ polymerization of a dopamine monomer in a mSi-dispersed basic solution using O_2 as an initiator (Figure 2a). The NHC layer was also directly encapsulated with negligible morphological difference via a coating process consisting of heat treatment at various temperatures under argon atmosphere (Figure 2b, c; Figure S1c-h, Supporting Information). Field-emission scanning electron microscope (FE-SEM) images with energy-dispersive spectroscopy (EDS) mapping showed that all the components of C, N, O, and Si were well distributed on the surface of the commercial mSi during overall processes, implying the successful formation of mSi@x-y (x = PDA, NHC-600, NHC-700, NHC-800, and y = 5, 10, and 20) active material

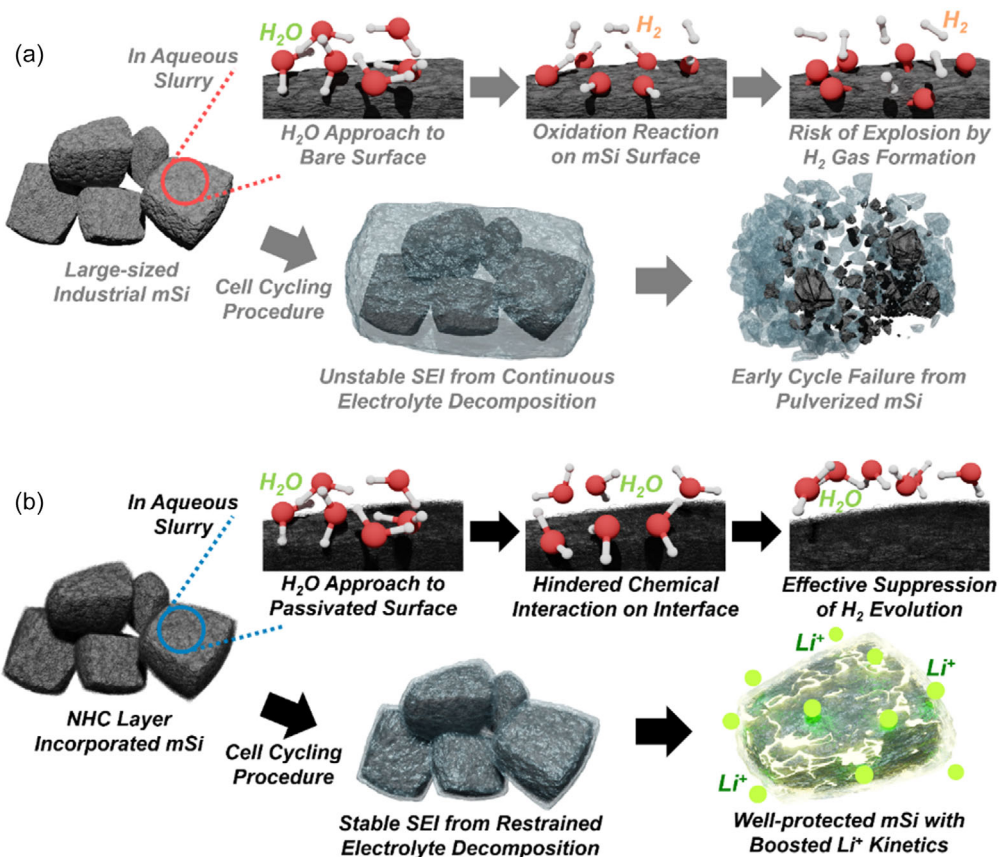


Figure 1. Schematic illustration of the electrode stability in terms of the safety issue of H₂ gas evolution and SEI construction on the anode surface. a) Bare mSi with continuously generated gas and unstable SEI. b) NHC layer decorated mSi with inhibited oxidation reaction on the surface and integrated robust SEI inducing enhanced Li⁺ kinetics.

(Figure 2d; Figure S2, S3a-d and S4a-c, Supporting Information). Transmission electron microscope (TEM) images demonstrated that thickness of a NHC layer (≈ 90 nm) on mSi@NHC-700-20 was less than that of a distinct PDA layer (≈ 200 nm) on mSi@PDA-20 because the carbonization process induced a compact hard carbon layer on the mSi surface (Figure 2e; Figure S5, Supporting Information).^[28] Thermal analyses of the samples were performed by thermal gravimetric analysis (TGA) and differential scanning calorimetry (DSC) experiments. The amounts of carbon contents on the mSi surface were analyzed by TGA in the air atmosphere for CO₂ release, which were estimated to be about 1.70, 2.54, and 3.51 wt% for the mSi@NHC-700-5, mSi@NHC-700-10, and mSi@NHC-700-20, respectively, indicating that the weight ratio of the added dopamine hydrochloride clearly affected the contents of the coating layer for the active material (Figure 2f). In agreement with the TGA results, the mSi@NHC-700-20 showed an exothermic peak with the highest energy of 408.3 J g⁻¹ (Figure 2g). The other mSi samples also displayed distinct peaks in TGA and DSC curves, and the similar TGA curve patterns between mSi@PDA-y and mSi@NHC-600-y suggested the incomplete carbonization of PDA layer due to the low temperature condition (Figure S6a-f, Supporting Information). The Brunauer–Emmett–Teller (BET) textural values of surface area, pore volume, and pore size of the mSi@x-y, as summarized in Table S1, Supporting Information, were revealed by N₂

adsorption–desorption isotherms (Figure 2h,i; Figure S7a-f, Supporting Information). The mSi@NHC-700-y and the mSi@NHC-800-y showed lower values of surface area ($1.8\text{--}7.9\text{ m}^2\text{ g}^{-1}$), pore volume ($32\text{--}74\text{ cm}^3\text{ g}^{-1}$), and pore diameter ($5.1\text{--}11.0\text{ nm}$) than those of the mSi@NHC-600-y in the range of $10.0\text{--}45.0\text{ m}^2\text{ g}^{-1}$, $0.013\text{--}0.058\text{ cm}^3\text{ g}^{-1}$, and $10.8\text{--}11.4\text{ nm}$. These results demonstrated that the higher temperatures are suitable to induce more compact and complete carbonized surface layer on the mSi, which was consistent with the TGA and DSC results. As revealed by the particle size distribution analysis, NHC coating process increased the size scale from $\approx 4.12\text{ }\mu\text{m}$ to $\approx 5.09\text{--}5.25\text{ }\mu\text{m}$ and decreased uniformity value of the mSi@NHC-700-y and mSi@NHC-800-y compared to that of mSi@NHC-600-y, implying that the uniform and compact carbonized layer was successfully covered on the mSi surface (Figure 2j; Figure S8; Table S2, Supporting Information). The mSi@NHC-700-20 showed a higher tap density than that of the mSi and mSi@PDA-20, which could be beneficial for practical application (Figure S9, Supporting Information).^[18] The higher carbonization temperature presented decreased D band to G band intensity ratio (I_D/I_G) as 0.96, 0.92, 0.91, and 0.89 for the mSi@PDA-10, mSi@NHC-600-10, mSi@NHC-700-10, and mSi@NHC-800-10, respectively, which indicates that the amorphous PDA layer was converted to a relatively graphite-like N-doped carbon structure (Figure 2k; Figure S10, Supporting

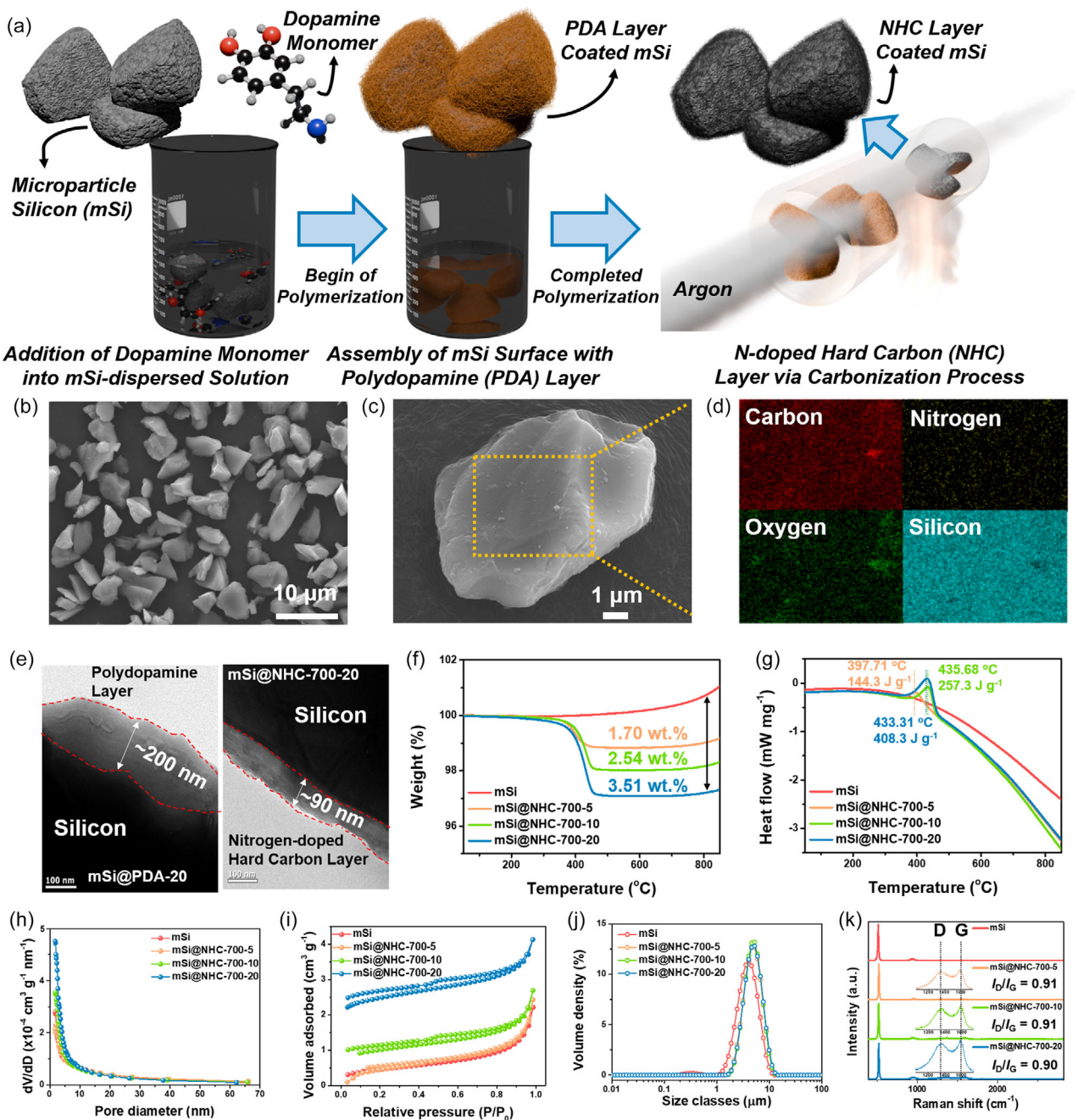


Figure 2. Synthesis and structural characteristics. a) Schematic showing the overall synthesis using wet chemical method and carbonization of PDA layer for direct-assembly of NHC with mSi. b,c) SEM image of mSi@NHC-700-20 with magnified version and d) corresponding EDS mappings. e) TEM images of mSi@PDA-20 (left) and mSi@NHC-700-20 (right). f) TGA analysis curves and g) corresponding DSC analysis data of the samples at the air condition. h,i) N₂ adsorption/desorption curves and pore size distributions of the samples, respectively. j) Particle size distribution data and k) Raman spectra of the samples.

Information).^[29] The Fourier transform infrared (FT-IR) spectra displayed C—O (1045 cm⁻¹), C=C/C—N (1539 cm⁻¹), and C—H (2847, 2920, and 2982 cm⁻¹) peaks, which were contributed by the chemical structure of the NHC layer on the mSi surface (Figure S11a-d, Supporting Information). Likewise, in small-angle X-ray scattering (SAXS) and wide-angle X-ray diffraction (WAXD) patterns (Figure S12a-f, Supporting Information), peak changes were observed for mSi@x-y powders in overall q ranges showing information of presence of micropores ($q < 0.04 \text{ \AA}^{-1}$) and macropores ($q > 0.3 \text{ \AA}^{-1}$).^[30-32]

Synchrotron-based high-resolution powder diffraction (HRPD) analysis, which was further conducted to verify the crystal structure of the various mSi powders, showed no gradual peak shift, revealing that the crystallography of the silicon structure was not affected by any chemical processes during the fabrication (Figure 3a-d; Figure S13a-i, Supporting Information). Moreover, Rietveld refinement results calculated from HRPD patterns also demonstrated similar d-spacing values in (111) direction as about 3.14 Å for all mSi@x-y (Table S3, Supporting Information). The chemical binding states of various species on the surface of

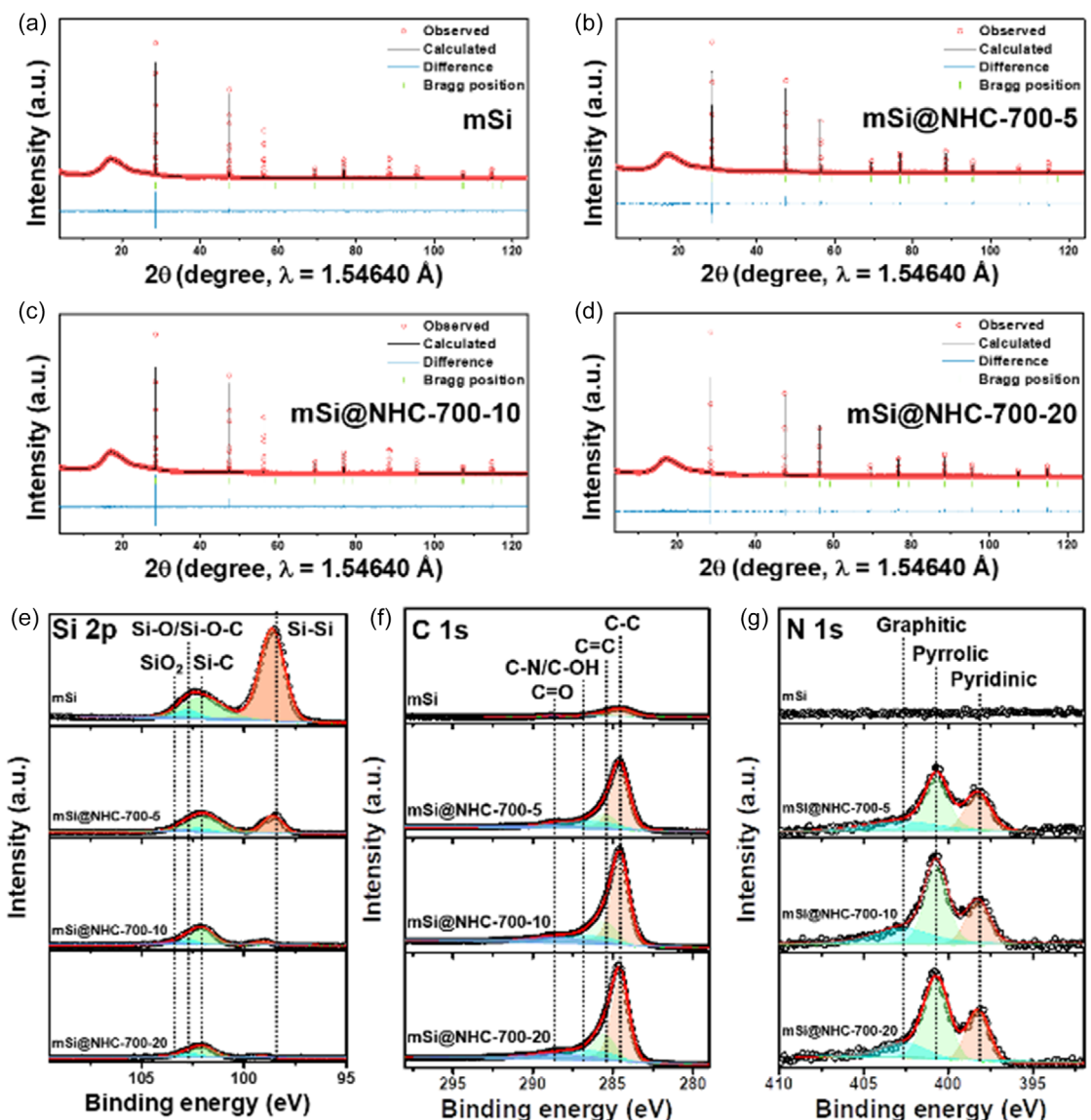


Figure 3. HRPD patterns with Rietveld refinement results of the a) bare mSi, b) mSi@NHC-700-5, c) mSi@NHC-700-10, and d) mSi@NHC-700-20. XPS spectra showing e) Si 2p, f) C 1s, and g) N 1s of the bare mSi, mSi@NHC-700-5, mSi@NHC-700-10, and mSi@NHC-700-20.

the mSi, mSi@NHC-700-5, mSi@NHC-700-10, and mSi@NHC-700-20 were investigated by X-ray photoelectron spectroscopy (XPS) showing four characteristic peaks of Si 2p, C 1s, and N 1s (Figure 3e-g; Table S4, Supporting Information). The diminished intensity values of Si 2p spectra, showing typical photoelectron peaks of Si–Si, Si–C, Si–O/Si–O–C, and SiO₂, revealed that the carbon matrix successfully covered the mSi surface.^[33,34] The C 1s spectra of C–C, C=C, C–N/C–OH, and C=O peaks and N 1s spectra of pyridinic-N, pyrrolic-N, and graphitic-N represented tendency to increase in values, which also obviously imply the formation of the NHC layer.^[17,33,35] The N-doped hard carbon obtained from commercial polymer pyrolysis shows a comparable I_D/I_G ratio in the Raman spectrum and identical chemical bonding states in the XPS spectra of C 1s and N 1s to those observed in the mSi@NHC-700-y samples. Therefore, these results provided clear evidences of the successful introduction of the NHC layer on the mSi.

2.2. Gas Generation Test During Preparation of Silicon Aqueous Slurry

The evolution of H₂ gas through the chemical oxidation of Si powders with water has been identified as a significant obstacle in industrial environments of water-based Si/CMC/Carbon mixtures resulting in H₂ safety risks, which is typically not be apparent during small-scale laboratory experiments.^[13,14] Therefore, the gas formation amounts of the mSi@x-y samples from aqueous slurries were monitored to evaluate whether the NHC coating on the mSi surface is an effective gas suppression strategy or not. Especially, an industrial-level slurry mixing process has been conducted in super-huge mixing equipment with capacity from 2300 to 3000 L scale for a long time exposed to an environment where heat generation can cause temperature increases during device operation. Therefore, we have set the overall experimental conditions as follows to closely replicate harsh conditions that may

pose risk factors occurring on a factory scale as much as possible at the lab scale; Each 5×10 cm scaled aluminum pouches had a 1.0 g scale of mSi@x-y/CMC/SWCNT/Graphitic-carbon slurry, and the well-sealed pouches were then placed at 50 °C oven and monitored for about 2 weeks for swelling behavior (representative sample photos in Figure S15a–m, Supporting Information), and the entire process is illustrated in Figure 4a. As shown in Figure S15a, Supporting Information, only the bare mSi sample significantly generated gas with the saturation after 2 weeks from 0 mL g^{-1} slurry to $10.2 (\pm 0.2) \text{ mL g}^{-1}$ slurry, and the other coated mSi samples did not show any swelling phenomenon (Figure 4b; Figure S16a–c, Supporting Information). It indicates that whether the PDA coating layer was carbonized or not, the Si oxidation reaction could be well hindered to suppress gas evolution during the slurry process by protecting the mSi surface from direct chemical contact with water. Subsequently, we applied the gas chromatography (GC) and mass spectroscopy (MS) methods to identify the type of evolved gas (Figure 4c–f). The concentration of H₂ gas was increased together with the gas generation from 72.4 (± 2.1) % (Day 3) to 88.4 (± 1.4) % (Day 13) (Figure 4c) and mass ion chromatogram signal of air, existing in the pouch, was steadily decreased for both of m/z 28 (N₂) and m/z 32 (O₂), revealing that the H₂ gas was the main evolved component which provoked the undesired oxidation reaction on the mSi surface with

no significant N₂/O₂ generation (Figure 4d–f).^[36] Furthermore, ex situ TGA, FT-IR, and XRD analyses of the fully dried slurry samples after the gas generation test revealed a clear phase transformation to SiO₂ in the bare mSi slurry sample, while no such transformation was observed in the mSi@NHC-700-y samples (Figure S17, Supporting Information). These findings suggest that mSi undergoes the following reaction under aqueous slurry conditions.



As a result, the scalable NHC coating process could be a reasonable choice to prevent H₂ safety issues and phase transformation to SiO₂ for the industrial use of the mSi anode.

2.3. Electrochemical Performances of the Prepared Anodes

To investigate the influence of the NHC layer on the electrochemical properties of the various anodes, the Nyquist plots of electrochemical impedance spectroscopy (EIS) tests were examined for the half-cells in pristine state and after 3 formation cycles at 0.15 A g⁻¹ (Figure 5a,b; Figure S18a–i, Supporting Information), and resultant fitting parameters are summarized in Table S5 and S6, Supporting Information. The EIS spectra typically consist

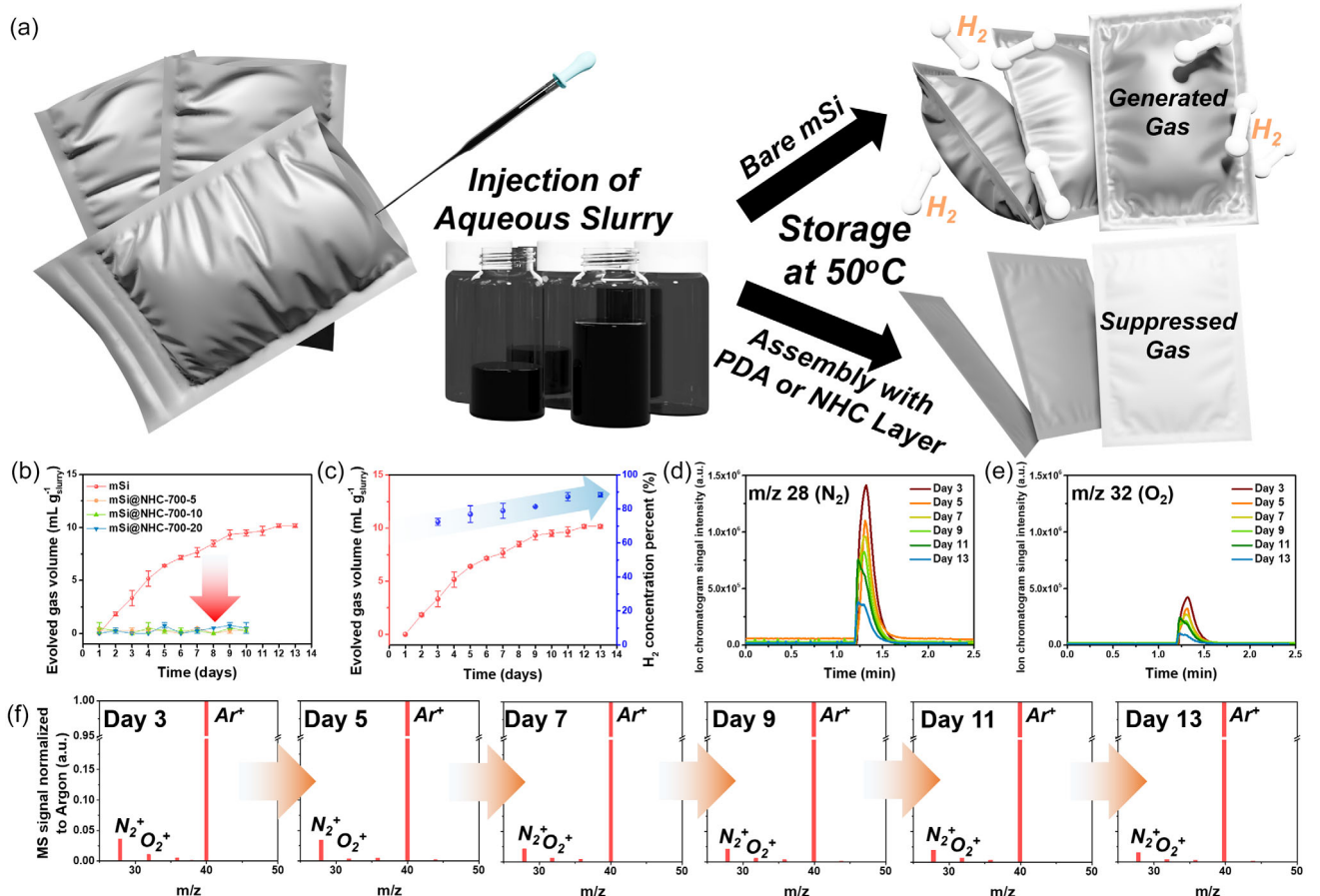


Figure 4. a) Schematic describing the process for gas evolution test. b) Time profile of gas formation from aqueous slurry of the mSi and mSi@NHC-700-y in sealed pouch. c) Calculated H₂ concentration in the evolved gas for the mSi. d,e) MS ion chromatogram intensity for m/z 28 (N₂) and m/z 32 (O₂) signals during 2 weeks, and f) specific time profile for N₂⁺, O₂⁺, and Ar⁺ components with normalized intensity according to Ar gas.

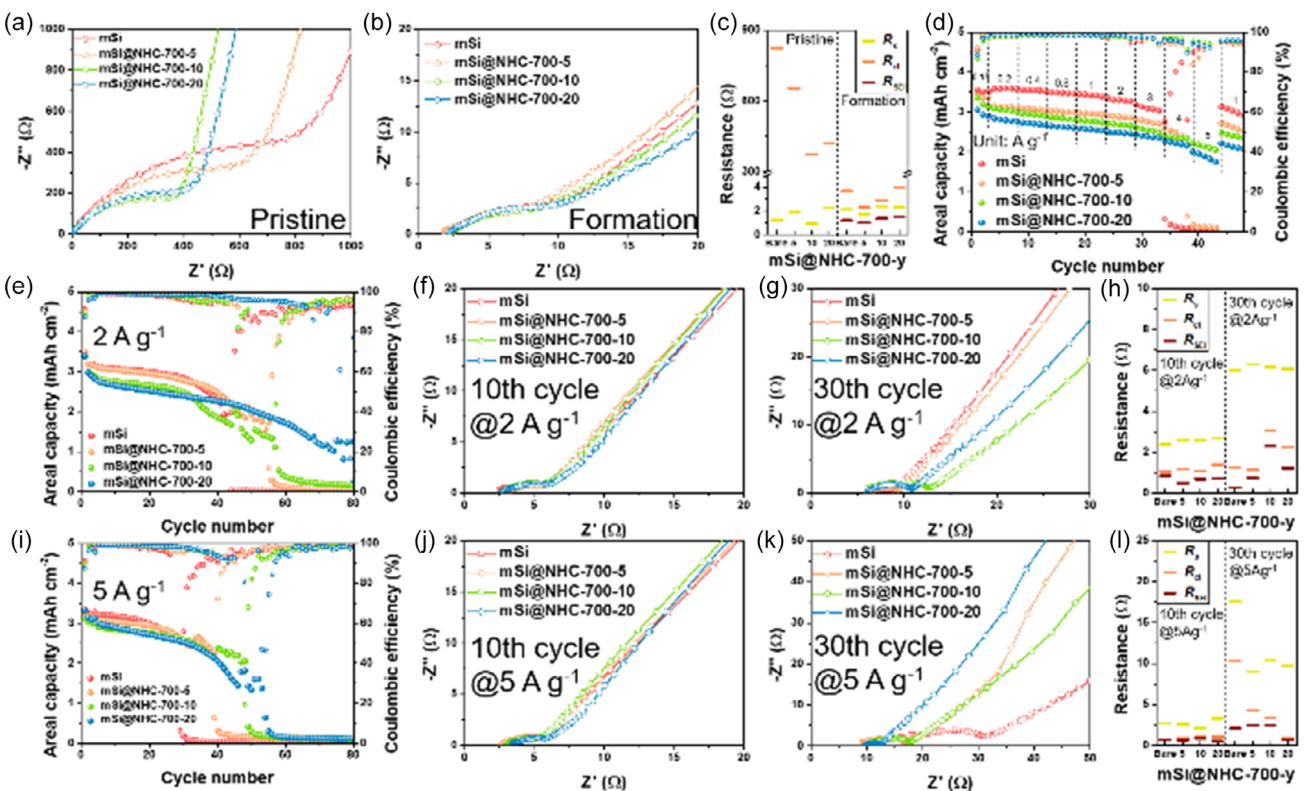


Figure 5. Electrochemical performances of the mSi and mSi@NHC-700-y electrodes. Nyquist plots of the impedance response a) at pristine state, and b) after formation process with c) quantitative analysis of the fitted EIS data. d) Rate capability performance. e) Cycling performance for 80 cycles at current density of 2 A g^{-1} and resultant Nyquist plots f) after 10th and g) 30th cycle with h) fitted EIS values. i) Comparable cycling test for 80 cycles at current density of 5 A g^{-1} and resultant Nyquist plots j) after 10th and k) 30th cycle with l) fitted EIS data.

of solution resistance (R_s), SEI impedance (R_{SEI}), charge transfer resistance (R_{ct}), and straight-sloped line at the low-frequency range.^[37,38] The R_{ct} values of all the fabricated cells were noticeably decreased after the formation cycling process, revealing the construction of effective SEI layer, which was also observed by additional interfacial resistance values (R_{SEI}) for enhanced charge migration between electrolyte and anodes (Figure 5c; Table S5 and S6, Supporting Information). The rate performance of mSi and mSi@NHC-700-y was shown in Figure 5d. The mSi electrode attained areal capacities of 3.58, 3.56, 3.49, 3.45, 3.35, 3.18, 2.76, 0.06, and 3.13 mAh cm⁻² at step-wise current densities of 0.2, 0.4, 0.8, 1, 2, 3, 4, 5, and 1 A g⁻¹, respectively, and the mSi@NHC-700-5 of 3.15, 3.08, 3.03, 2.98, 2.91, 2.82, 2.60, 0.18, and 2.72 mAh cm⁻², mSi@NHC-700-10 of 3.09, 2.97, 2.87, 2.80, 2.72, 2.61, 2.39, 2.21, and 2.48, and mSi@NHC-700-20 of 2.84, 2.73, 2.65, 2.59, 2.51, 2.43, 2.28, 2.01, and 2.22 mAh cm⁻², respectively. In other words, the mSi@NHC-700-y anodes delivered a decreased discharge capacity than the bare mSi electrode at low current densities ($0.2\text{--}3 \text{ A g}^{-1}$), which might be attributed to relatively low initial Coulombic efficiency (ICE) value in the formation process due to the increased BET surface area from the NHC layer for additional reactions.^[39–42] It demonstrated as of 90.07 (± 0.36) %, 88.99 (± 0.24) %, and 87.03 (± 0.32) % for the mSi@NHC-700-5, mSi@NHC-700-10, and mSi@NHC-700-20 anode, which were lower than that of the mSi showing 91.19 (± 0.18) % (Figures S19a–n and S20a–d, Supporting Information). On the other hand, they could

effectively maintain their rate capabilities even at high current densities ($4\text{--}5 \text{ A g}^{-1}$), which could be associated with the enhanced electronic/ionic conductivity due to the NHC layer.^[16,18] Therefore, a possible trade-off relationship between the conductive contribution and decrease of ICE arose by the NHC layer should be addressed to precisely identify the advantages of the carbon coating strategy on overall electrochemical performances. Therefore, we conducted long cycling tests for representative two cases at (i) 2 A g^{-1} and (ii) 5 A g^{-1} (Figure 5e–p). As the weight fraction of NHC layer was increased, the mSi@NHC-700-y electrode exhibited more stable cycling performances at current density of 2 A g^{-1} where the mSi@NHC-700-5, mSi@NHC-700-10, and mSi@NHC-700-20 showed reinforced reversible areal capacities of 1.74 mAh cm⁻² for 55th cycle, 1.11 mAh cm⁻² for 57th cycle, and 1.26 mAh cm⁻² for 79th cycle before cell failure, respectively, whereas the bare mSi delivered rapid capacity decay at the same condition in spite of low overall resistance components in the early stage (Figure 5e–h; Table S7, Supporting Information). At current density of 5 A g^{-1} , the bare mSi underwent severe capacity decay even after 29 cycles, while the mSi@NHC-700-y anodes displayed stable capacity maintenance achieving 2.26 mAh cm⁻² at 39th cycle, 2.05 mAh cm⁻² at 48th cycle, and 1.38 mAh cm⁻² at 53th cycle for the mSi@NHC-700-5, mSi@NHC-700-10, and mSi@NHC-700-20, respectively (Figure 5i). These electrochemical evaluations of the mSi@NHC-700-y electrodes, especially for mSi@NHC-700-20, also showed better cyclic stability compared

to those of the other mSi@PDA-y, mSi@NHC-600-y, and mSi@NHC-800-y, revealing that optimal carbonization condition should be considered (Figure S21–S27, Supporting Information). The noisy Coulombic efficiency data observed with the rapid decrease in discharge capacity during cycling can be attributed to continuous anode volume expansion, leading to electrolyte depletion and lithium consumption. Even when the criterion was changed to specific capacity, the anodes exhibited the same trend in results with the best cycling stability at the mSi@NHC-700-20 electrode (Figure S28, Supporting Information). The difference in values of the R_s , R_{ct} , and R_{SEI} at 5 A g^{-1} among the electrodes was noticeably changed after 30th cycle (Figure 5j–l; Table S8, Supporting Information). Particularly, the R_s value for mSi@NHC-700-20 varied from 3.32 to 9.75 Ω , indicating a smaller change compared to the mSi electrode, which varied from 2.69 to 17.6 Ω . This difference could be explained by effectively overcoming ohmic polarization with conductive NHC layer when Li^+ ions interacted with the active material covered by the SEI in the electrolyte.^[43] Moreover, the mSi@NHC-700-20 also displayed lower changed R_{ct} (from 1.02 to 2.24 Ω) and R_{SEI} (from 0.498 to 1.58 Ω) values than mSi, which exhibited changed R_{ct} (from 0.724 to 10.3 Ω) and R_{SEI} (from 0.676 to 2.12 Ω) values, suggesting that the mSi@NHC-700-20 electrode allowed charges to easily overcome activation polarizations when entering the SEI layer and migrating to the mSi.^[16,43] In addition, the straight line of the mSi@NHC-700-20 electrode demonstrated a steeper slope than that of the bare mSi electrode, implying faster Li^+ diffusion dynamics attributed to synergy between the proper NHC layer and SEI components to induce superior ionic conductivity.^[44] In dQ/dV curves, although peak positions of the mSi@NHC-700-20 at 1st, 10th, 20th, and 30th relatively kept the constant, those of the mSi continuously shifted as the cycle proceeded, indicating that the NHC layer produced more stable SEI which could reduce loss of capacity and polarization on electrode (Figure S29, Supporting Information).^[41,45] Moreover, increased and well-maintained Coulombic efficiency of the mSi@NHC-700-20 over that of mSi was observed after several cycling (Figure S30, Supporting Information), indicating suppressed side reactions with the electrolytes due to stable SEI which reduced the new formation of Si surface and severe electrolyte decomposition.^[16,18] Thus, these results possibly highlighted the efficiency of the NHC coating layer for facile transport of ions/electrons and formation of stable SEI layer enhancing lithiation/delithiation kinetics and cyclic stability even at high current densities.^[44] Moreover, it suggested an effective mitigation of possible volumetric expansion of mSi through carbon coating strategy,^[18] which could be verified by long cycling performances of the mSi@PDA-y anodes showing similar stability compared to those of the bare mSi (Figure S22 and S24). Similarly, under a condition at a very low current density of 1 A g^{-1} , the mSi@NHC-700-20 anode showed the highest stability with 35.2 % retention value for 120 cycles (Figure S31, Supporting Information). Considering relatively larger size of commercial-level mSi in this work, the anodes showed competitive electrochemical performances in terms of Si loading, capacity, and ICE values compared to those of recently studied micro-sized Si-based composite anodes (Table S9, Supporting Information).

2.4. Charge Diffusion Kinetics of the Prepared mSi Anodes

With boosted cyclic stability from introduction of the NHC layer that enables high electronic transport, underlying charge transport properties should be revealed for clear understanding.^[15] Therefore, charge diffusion interactions were characterized in half cells by galvanostatic intermittent titration technique (GITT) and cyclic voltammetry (CV) methods which were performed to further reveal kinetic behavior of lithiation/delithiation reaction in various SOC/DOD states.^[46] At first, the GITT was used to determine the Li^+ chemical diffusion coefficients in the mSi@NHC-700-y electrodes by applying a constant current flux for a limited time period at the first cycle after formation process (Figure 6a–d). The Li^+ diffusion coefficient (D_{Li^+}) in the mSi@NHC-700-y anodes was larger than that of the bare mSi anode in every tested lithiation (Figure 6e,f) and delithiation (Figure 6g,h) states, indicating that the highly conductive NHC layer effectively formed ionic pathway with faster lithiation kinetics and shorter time to be stabilized when no external potential was applied.^[47,48] In addition, the first three CV curves of the mSi and mSi@x-y anodes at a scan rate of 0.1 mV s^{-1} were analyzed (Figure 6i,j; Figure S32a–k, Supporting Information). During the first cathodic operation, evident peaks at about 1.3 V (vs. Li/Li^+) were observable which were attributed to irreversible reaction between anode and electrolyte forming the SEI layer. The other cathodic peak, attributed to the phase transition from crystalline Si to the Li_xSi alloy, was recorded at 0.148 V for the mSi@NHC-700-20, indicating higher reactivity compared to mSi, mSi@NHC-700-5, and mSi@NHC-700-10, which exhibited peaks at 0.128, 0.139, and 0.146 V, respectively. Similarly, two anodic peaks corresponding to the delithiation of amorphous Li_xSi to the Si phase were observed at 0.379 and 0.545 V for mSi@NHC-700-20, comparable to those of mSi@NHC-700-5 and mSi@NHC-700-10.^[44] On the other hand, the mSi anode showed only one right-shifted prominent peak at 0.584 V due to the sluggish phase transition resulting from poor ionic conductivity.^[49] The Li^+ transport kinetics were also investigated by CV curves where peak currents of each points were fitted to show a linear tendency using Randles–Sevcik equation (Figure 6k–m; Figure S33a–n, Supporting Information). The Li^+ diffusion coefficient ($aD^{1/2}$) calculated for the mSi@NHC-700-20 electrode displayed slope values of 1.03 for the anodic peak and 1.34 for the cathodic peak, which were higher than those of the mSi@NHC-700-5 and mSi@NHC-700-10 electrodes, with 0.45 and 0.97 for anodic peaks, and 0.58 and 1.24 for cathodic peaks, respectively, in a good agreement with previous electrochemical results. Oppositely, the mSi anode showed the lowest values as 0.43 and 0.55 for anodic and cathodic peaks, respectively, indicating that the coated NHC layer could play a crucial role in increasing Li^+ transport by boosting overall electronic and ionic conductivity.^[50] The different diffusion coefficients analyzed by the GITT and CV techniques were due to the different equilibrium conditions and essential parameters.^[51–53] Similarly, the other electrodes also displayed improved Li^+ mobility kinetics but lower than that of mSi@NHC-700-y anodes (Figure S33c–n, Supporting Information). Furthermore, a surface-dominated capacitive characteristic could be revealed by the positively shifted peak potential to a higher

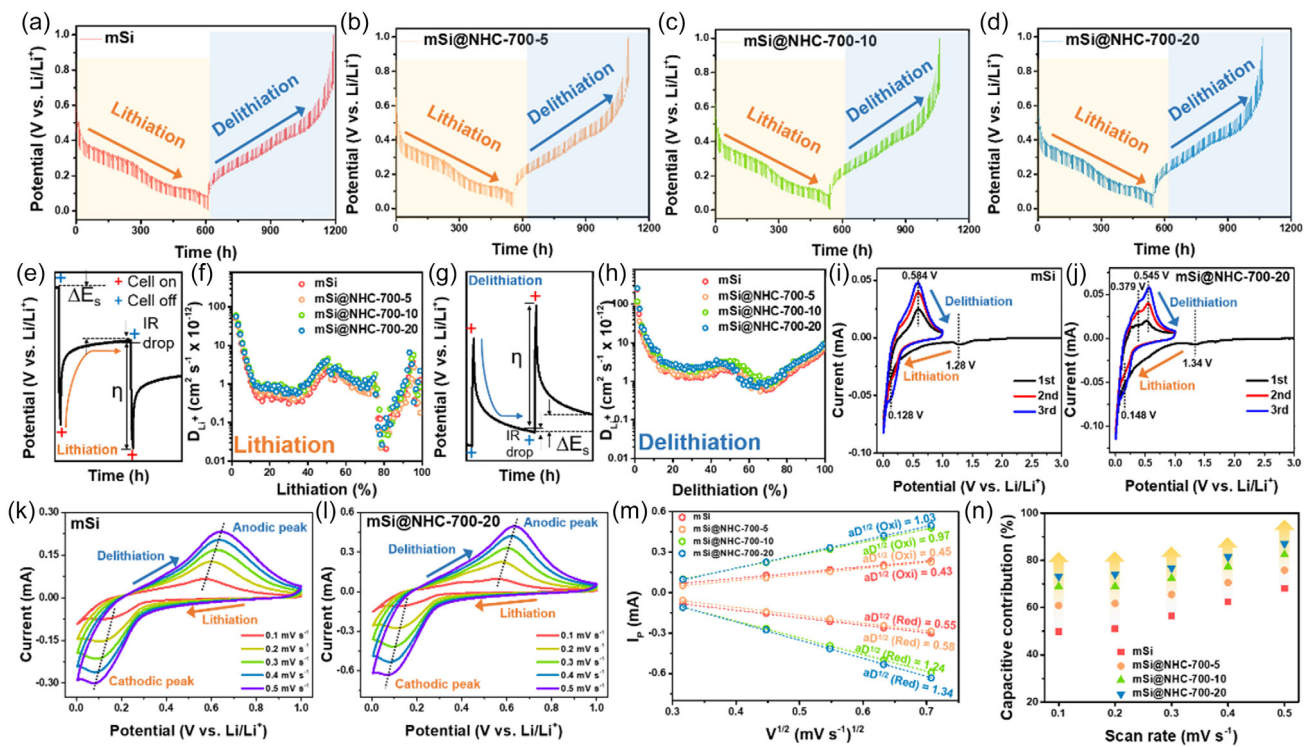


Figure 6. Charge transport kinetics of various anodes. GITT curves in voltage from 0.005 V to 1.0 V at 1st cycle after formation process of a) mSi, b) mSi@NHC-700-5, c) mSi@NHC-700-10, and d) mSi@NHC-700-20. Corresponding partial zoom-in curves and calculated Li^+ diffusion coefficient during the different e,f) lithiation and g,h) delithiation states of the samples. Various CV curves with anodic/cathodic peaks at 0.1 mV s^{-1} for i) mSi and j) mSi@NHC-700-20 anodes, and at different scan rates from 0.1 to 0.5 mV s^{-1} for k) mSi and l) mSi@NHC-700-20 anodes. m) The fitted lines with linear relationship between redox peak currents versus the square root of the scan rate at reduction and oxidation processes. n) Different capacitive contributions at various scan rates for the anodes.

value,^[54,55] and the capacitive-contributed current can be obtained via Dunn method for CV kinetics analysis using a normalization formula (Figure S34, Supporting Information):

$$i(V) = k_1 v + k_2 v^{1/2} \quad (2)$$

where i is the peak current, V is the potential, v is the scan rate (mV s^{-1}), and the values of k_1 and k_2 are used to distinguish the capacitive and diffusion currents.^[56] The ratios of capacitive-controlled contribution in the current values of all the electrodes were gradually increased as the charge-storage process at high current density could not be influenced by sluggish Li^+ diffusion (Figure S35–S47, Supporting Information).^[57,58] The capacitive fractions were remarkably increased at all scan rates proposing that the assembly with spatially homogeneous and highly conductive NHC layer could facilitate efficient Li^+ storage with the high specific surface area for a kinetically boosted charge transport during the charge/discharge process attributed to a capacitive property of hard carbon, which possibly suggested that the synergistic effect was optimally applied to the mSi@NHC-700-20 thereby enabling the most stable cyclic performance (Figure 5a–n and 6n; Figure S48b,c, Supporting Information).^[42,59] On the other hand, the mSi@PDA-y anodes showed poor capacitive contribution value comparable to that of the bare mSi, emphasizing the importance of carbonization process of PDA layer to enhance the surface-controlled currents (Figure S48a, Supporting Information).

2.5. Physicochemical Post-Mortem Analysis of the Anodes After Cycling Process

A micro-sized Si typically provokes the large volume expansion inducing severe swelling of anodes which hinder long-term cyclic stability. In this regard, the surface roughness and morphological change of the anodes were observed after 30 cycles at different current densities to investigate the high structural integrity induced from the NHC layer using ex situ atomic force microscopy (AFM) images, top-view and corresponding cross-sectional SEM images (Figure 7; Figure S49 and S50, Supporting Information). According to the analyzed AFM results, the mSi@NHC-700-20 electrode demonstrated a smoother surface at both current density of 2 A g^{-1} and 5 A g^{-1} showing root mean square (RMS) roughness values of 99.2 and 212.1 nm, respectively, which were lower than those of the bare mSi electrode showing 182.5 and 227.7 nm, respectively (Figure 7a). The different roughness was also validated by SEM images (Figure 7b). The top-view SEM images showed similar surface structures for the mSi and mSi@NHC-700-y anodes before cycling. After 30 cycles, evidently diminished mechanical damages of cracks and fractures for the mSi@NHC-700-5, mSi@NHC-700-10, and mSi@NHC-700-20 anodes were observed at both 2 A g^{-1} and 5 A g^{-1} . Moreover, the corresponding cross-sectional SEM images demonstrated that the thickness of the mSi electrode was significantly increased by 130.9% (18.1–41.8 μm) and 253.0% (18.1–63.9 μm) at the current density of 2 A g^{-1} and 5 A g^{-1} , respectively. In comparison,

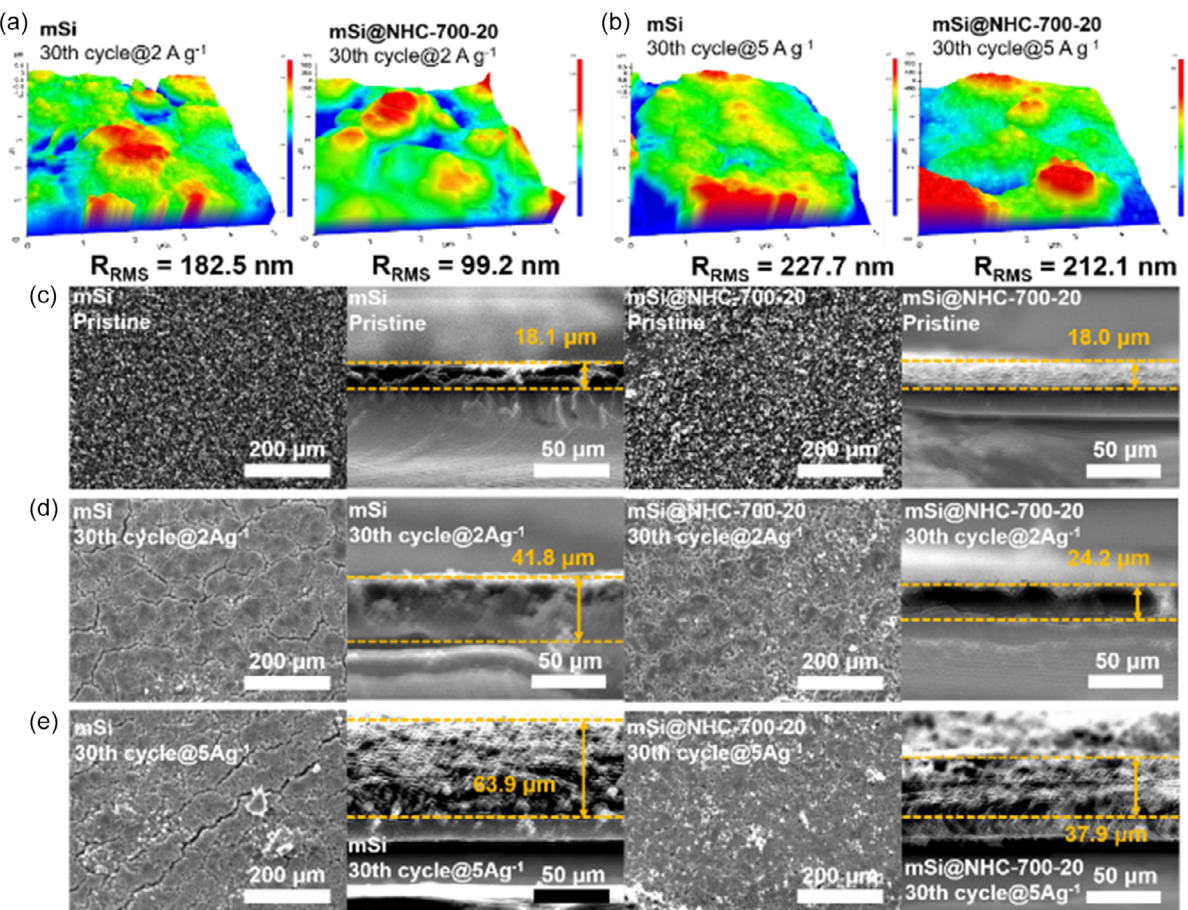


Figure 7. Post-mortem analysis after subsequent lithiation/delithiation process. AFM 3D morphology images of mSi and mSi@NHC-700-20 electrodes after 30th cycle at different current density of a) 2 A g^{-1} and b) 5 A g^{-1} . c) Top-view and corresponding cross-sectional SEM images of mSi and mSi@NHC-700-20 electrodes at the states c) in pristine, and d) after 30th cycle at 2 A g^{-1} and e) 5 A g^{-1} rates.

the mSi@NHC-700-20 electrode showed the remarkable lowest values of 34.4 % ($18.0\text{--}24.2 \mu\text{m}$) and 110.6 % ($18.0\text{--}37.9 \mu\text{m}$) under 2 A g^{-1} and 5 A g^{-1} current density conditions, respectively, after 30 cycles. Likewise, the mSi@NHC-700-5 and mSi@NHC-700-10 anodes also showed the improved stability properties in the electrode level (Figure S49, Supporting Information). Therefore, it is ascertaining that the conductive NHC assembled on mSi surface could serve as a buffering layer preserving the integrity of the anode during subsequent lithiation/delithiation process, which was also verified by considering that precarbonized PDA layer was disadvantageous for structural stability (Figure S50, Supporting Information), in a good agreement with the long cycling performance of the mSi@PDA-y anodes (Figure S21–S27, Supporting Information). Ex situ XPS analysis on the mSi and mSi@NHC-700-y electrodes after cycling processes was conducted to further elucidate the correlation between chemical composition of SEI layer and electrochemical performance of the cells (Figure S51, Supporting Information), providing several peaks of similar organic and inorganic components. Especially for the C 1s and Li 1s spectra, higher contents of the LiF and Li_2CO_3 for the mSi@NHC-700-20 anode revealed that the continuous decomposition of electrolyte after initial SEI formation was hindered during 15 cycles at current density of 5 A g^{-1} ,^[60] in

consistent with the trend in P 2p spectra demonstrating lower content of Li_1PF_y due to the restrained reduction of electrolyte toward more stable SEI layer (Figure S52, Supporting Information).^[61] Moreover, the abundant LiF-containing SEI with the existence of Li_2CO_3 could accelerate kinetics of the lithiation/delithiation process, induce uniform Li^+ flux, and relieve volume variation.^[18,61,62] This chemical distribution could be also explained by dipole-dipole interaction through hydrogen bonding between positively charged N species and generated LiF components.^[16,63] The similar intensity of the peaks at 2 A g^{-1} after 15 cycles might indicate that a SEI induced by higher ICE for bare mSi temporarily facilitated reversible Li^+ usage before electrolyte degradation in an early cycling time, as demonstrated in Figure S30, Supporting Information.^[40,59] Therefore, an assembly of the highly efficient NHC with a surface of the mSi can effectively improve the physicochemical properties of the SEI even under the fast charging/discharging condition with inhibition of internal cracks for the electrodes toward stable long-term cycling performance.

2.6. Achievement of Highly Stable Full Cell Systems

To further verify the commercial potential of the scalable NHC coating strategy under practical conditions, coin-type

full cells were fabricated combining with a high loading $\text{LiNi}_{0.65}\text{Co}_{0.15}\text{Mn}_{0.20}\text{O}_2$ (Ni65, $\approx 11 \text{ mg cm}^{-2}$, $\approx 2.13 \text{ mAh cm}^{-2}$) cathode to satisfy N/P ratio as ≈ 1.6 . All the electrochemical tests included the three precycling process at 0.05 C rate. First, the assembled full cells were evaluated under asymmetrical condition at 1 C ($\approx 2.2 \text{ mA cm}^{-2}$) charge and 0.5 C ($\approx 1.1 \text{ mA cm}^{-2}$) discharge rates to imitate a harsh and practical use of LIBs. The various full cells demonstrated a similar pattern in ICE, corresponding to the type of assembled anodes used (Figure S53, Supporting Information). Up to 150/300 cycles, the mSi@NHC-700-y||Ni65 cells clearly achieved higher areal capacities with retention rates of 44.8%/27.7%, 45.5%/27.8%, and 43.8%/27.9% for the mSi@NHC-700-5||Ni65, mSi@NHC-700-10||Ni65, and mSi@NHC-700-20||Ni65, respectively. These results surpassed retention rates of the mSi||Ni65 cell, which showed 41.6%/27.3% (Figures S54a-f and S55a-g, Supporting Information). Moreover, when the current density was increased to 3 C ($\approx 6.6 \text{ mA cm}^{-2}$) charge/discharge rate, the electrochemical performances showed apparent difference among the various full cells. Specifically, the mSi@NHC-700-20||Ni65 cell achieved retention values of 47.9% and 32.6% after 150 and 300 cycles, respectively, outperforming the mSi||Ni65, mSi@NHC-700-5||Ni65, and mSi@NHC-700-10||Ni65 cells, which delivered 33.8%/23.1%, 39.0%/25.1%, and 37.5%/28.7%, respectively (Figure 8a,b; Figures S56a-d and S57a-g, Supporting Information). This trend persisted at ultrafast charge/discharge rates of 6 C ($\approx 13.2 \text{ mA cm}^{-2}$) and 10 C ($\approx 22.0 \text{ mA cm}^{-2}$) (Figure S58a-l, S59a-f, and S60a-h, Supporting Information). This achievement is comparable with long-term cycling performances of

coin-type full cells accompanied with various size of Si anodes proposed in the previous literatures, as the mSi@NHC-700-20||Ni65 cell attained values of capacity decay per cycle as 0.24% and 0.22% under 1C/0.5C and 3C/3C rate conditions, respectively (Figure 8c).^[16,22,24,64–73,75] Due to widely known interfacial side reactions of dissolved transition metal species (Ni, Co, and Mn) migrating from the NCM cathode to the mSi anode during cycling, structural integrity should be considered not only for anode but also for cathode to evaluate full cells due to potential influence from cathode degradation.^[18] As shown in synchrotron-based in situ X-ray diffraction (XRD) spectra, shifts of the (003) peak were determined to be 0.07° and 0.04° during the H2-H3 phase transition for the cathodes of the mSi||Ni65 and mSi@NHC-700-20||Ni65 cells, respectively, in the initial cycle at 0.75 C (Figure S61a-b, Supporting Information).^[74,75] Additionally, relative changes in the lattice parameter c of the mSi@NHC-700-20||Ni65 full cell became smaller with continuous charge/discharge cycles at both 0.75 C and 3 C rates (Figure S62a-f, Supporting Information).^[76,77] These results might demonstrate the practical feasibility of integrated NHC layer system for stabilized cathode side. Moreover, the decreased interphase resistances of the mSi@NHC-700-y||Ni65 demonstrated that the surface modification with conductive NHC could provide a beneficial interface for the effective transfer of charge carriers (Figure S63, Supporting Information).^[18] These results demonstrated a great potential for the synergistic use of the NHC as an integrated material with mSi anode for practical advanced application such as energy storage systems and next-generation LIBs.

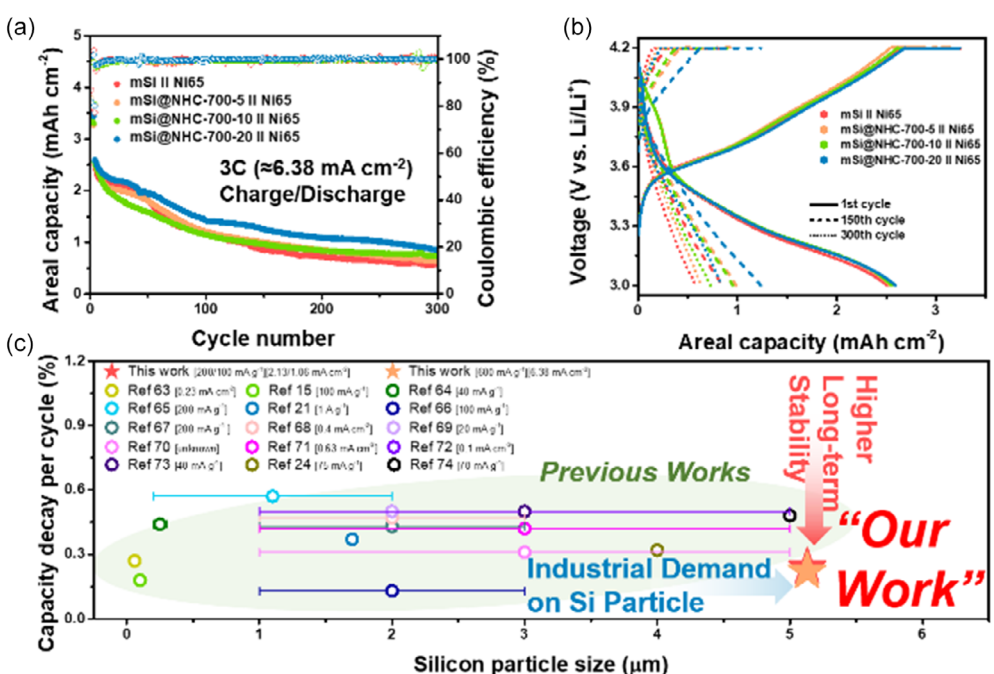


Figure 8. Electrochemical evaluation in practical coin-cell type full cell battery systems. Cycling performance of the mSi||Ni65, mSi@NHC-700-5||Ni65, mSi@NHC-700-10||Ni65, and mSi@NHC-700-20||Ni65 full cells for 300 cycles and corresponding galvanostatic charge/discharge profiles at 1st, 150th, and 300th cycle at a,b) 3 C charge/3 C discharge conditions. c) Comparison of electrochemical performances for mSi@NHC-700-20||Ni65 measured in this work and previously reported representative various microparticle Si-based coin-type full cell systems, expressed in terms of Si particle size (μm) and capacity decay per cycle (%).

3. Conclusion

In summary, we introduced a highly conductive NHC-layered structure on industrial demanded large-sized mSi of $\approx 5\text{ }\mu\text{m}$ through a facile and scalable direct wet-chemical coating technique of PDA followed by carbonization process. The entire fabrication process was focused on multi-gram scale, suggesting potential for extending to larger systems where the mSi and dopamine monomer are capable of being mixed. The optimally developed compact nitrogen-rich layer facilitated effective passivation on the mSi/electrolyte interface, inhibiting oxidation reactions on the mSi surface and consequently preventing H_2 gas generation from aqueous slurry, which is advantageous for resolving industrial gas explosion issues. Additionally, the NHC layer facilitated rapid Li^+ flux with active nitrogen sites, inducing superior ionic/electronic conductivity and capacitive contribution for enhanced electrochemical performances. Furthermore, the resultant integrated system provided robust solid physical support which alleviated volumetric expansion toward improved structural integrity of active material particles and effective stress tolerance of electrodes, thereby reducing detrimental electrolyte decomposition on continuously produced mSi surface and allowing robust SEI formation with enriched LiF and Li_2CO_3 phase components. Attributed to the enhanced structural and electrochemical features of the system, the rationally designed, straightforward, and scalable coating approach for the conductive NHC protective layer on mSi surface exhibited outstanding cyclic stability in a coin-type full cell system pairing with the NCM651520 cathode with areal capacities over 0.85 mAh cm^{-2} and 0.84 mAh cm^{-2} even after 300 cycles under a harsh condition of 1 C charge/0.5 C discharge and a fast condition of 3 C charge/3 C discharge, showing capacity decay rates of only 0.24% and 0.22%, respectively. We believe that our commercial-level accepted strategy of direct surface modification on the road to multifunctional stable nanolayer could highlight a promising way to fulfill the rising demands for high-energy-density anodes in next-generation LIBs.

4. Experimental Section

Materials and Chemicals

Micro-sized silicon particles (mSi, $\approx 5\text{ }\mu\text{m}$, LG Energy Solution), dopamine hydrochloride ($(\text{HO})_2\text{C}_6\text{H}_3\text{CH}_2\text{CH}_2\text{NH}_2\text{HCl}$, Sigma Aldrich), hydrochloric acid (HCl, 35%–37%, Samchun Chemicals), tris(hydroxymethyl)aminomethane (99.8–100.1%, Thermo Fisher Scientific), and carboxymethyl cellulose (CMC, MTI) have been used in this study. The $\text{LiNi}_{0.65}\text{Co}_{0.15}\text{Mn}_{0.20}\text{O}_2$ (NCM651520, Ni65) electrode was provided by LG Energy Solution; it consists of aluminum foil, active material, carbon, and binder. All the reagents were used without any further purification. Deionized (DI) water (resistivity $> 18\text{ M}\Omega$) was used for all experimental procedures.

Preparation of Scalable N-doped Carbon-Coated Silicon Microparticle

First of all, tris buffer solution (0.01 M) was fabricated by dissolving tris(hydroxymethyl)aminomethane powder in DI water (500 mL)

and was adjusted to pH of 8.5 by adding HCl solution dropwise. After that, mSi (5.0 g) was dispersed into the solution with continuous stirring for 12 h, and the solution was ultrasonicated for 0.5 h to induce emulsion. Subsequently, dopamine hydrochloride was added and mixed under magnetic stirring for 24 h in air atmosphere for polymerization. The polydopamine (PDA)-coated mSi powder was collected by vacuum filtration and dried. The obtained samples were carbonized at specific temperatures under argon atmosphere for 2 h at a ramping rate of $1\text{ }^\circ\text{C min}^{-1}$. All of samples were labeled as mSi@x-y, where x is carbonization condition (PDA, NHC-600, NHC-700, and NHC-800 for no calcination, 600 °C, 700 °C, and 800 °C) and y is weight percent of added dopamine hydrochloride (0.26 g, 0.56 g, and 1.25 g for 5 wt%, 10 wt%, and 20 wt%) relative to the weight scale of mSi powder. The various mSi samples were used for further investigation after each had accumulated a minimum weight of 25 g and were thoroughly mixed.

Material Characterization

The morphology and atomic distribution of mSi samples were examined using TEM (JEM-2200FS; JEOL) at 200 kV and FE-SEM (S-4800; Hitachi) with EDS at 15 kV. XPS (K-Alpha⁺; Thermo Fisher Scientific) analysis was carried out with a monochromatic Al-K α source ($E = 1486.6\text{ eV}$). Thermal decomposition data were obtained using TGA and DSC (SDT Q600; TA instruments). The BET method was applied using N_2 adsorption-desorption (ASAP 2020 BET/porosimeter; Micromeritics). FT-IR (Spectrum Two FT-IR Spectrometer; PerkinElmer) signals were recorded as transmittance spectra. The Raman spectrophotometer (NRS-5100; JASCO) was equipped with a 532 nm excitation laser of notch. Particle size distribution data were collected using particle analyzer (Master sizer 2000, Malvern). AFM observation was conducted to determine the physical properties of the anode surface after the 30th cycle (NX20; Park Systems) with noncontact surface roughness measurements mode. Crystal structure was investigated by Rietveld refinement which was performed using synchrotron HRPD patterns obtained at the 9B HRPD beamline of the Pohang Light Source (PLS-II) with a monochromatic X-ray wavelength of 1.54640 \AA . SAXS/WAXD experiments were conducted at the 6D C&S UNIST SAXS beamline of PLS-II with a wavelength of 1.07216 \AA and a 11.564 keV X-ray energy.

Gas Evolution Test of Aqueous Slurry

Slurries were mixtures of mSi@x-y (0.24 g), single-wall carbon nanotube (SWCNT) solution (0.4 wt% of SWCNT and 0.6 wt% of CMC in DI-water, 3.0 g), additional binder (12.7 wt% in DI-water, 0.094 g), and graphitic conductive agent (0.018 g). The mixture was divided into thirds and put into the aluminum pouch samples ($5 \times 10\text{ cm}$), which were sealed and contained in an oven maintained at $50\text{ }^\circ\text{C}$. The volume change was measured every day at the same time. The amount of evolved H_2 gas was analyzed during heating by a gas chromatograph (GC, 7890 A; Agilent Technologies) equipped with a thermal conductivity detector (TCD), and that of other gases was monitored by mass spectroscopy (MS, 5977B MSD; Agilent Technologies). An ex situ gas injection technique was used for overall gas analysis.

Electrochemical Measurements

The same slurry used in the gas evolution test was cast onto a copper foil, then dried at $80\text{ }^\circ\text{C}$ for 6 h under vacuum for anode electrodes. The mass loading of active materials with circular diameter of 14 mm was about 1.0 mg cm^{-2} . Typical CR2032-type coin cells were assembled in an argon-filled glove box and tested on a battery system (WBCS 3000; Won-A Tech) strictly maintained at $25\text{ }^\circ\text{C}$. Metallic lithium foil of 19 mm diameter was used as a counter electrode with 1 M lithium hexafluorophosphate (LiPF_6) dissolved in ethylene

carbonate/ethyl methyl carbonate (EC/EMC) (3:7 v/v) with 10 % fluoroethylene carbonate (FEC) as an electrolyte, and commercial polypropylene film (Celgard 2400) as a separator for half-cell test. A full cell included the Ni65 electrode (2.2 mAh cm⁻²) of 12 mm diameter as a cathode which is controlled to have N/P ratio of ≈1.6. The galvanostatic charge-discharge test was conducted over a voltage range of 0.005–1.0 V (vs. Li/Li⁺) for the half-cell and 3.0–4.2 V (vs. Li/Li⁺) for the full cell at various current rates. CV was conducted with the same voltage range at multiple scan rates from 0.1 to 0.5 mV s⁻¹, and Li⁺ diffusion coefficient was calculated based on Randles–Sevcik equation:

$$i_p = 0.4463nFAC\sqrt{\frac{nFvD}{RT}} \quad (3)$$

where i_p , n , F , and A are peak current, number of electrons, Faraday constant, and surface area of electrode, respectively. v , D , R , and T indicate scan rate, Li⁺ diffusion coefficient, gas constant (8.314 J mol⁻¹ K⁻¹), and temperature (K), respectively. Under the same experimental conditions, values of n , F , A , C , R , and T could be constant, and we can simplify the equation:

$$i_p = a\sqrt{Dv} \quad (4)$$

where a is a constant and $aD^{1/2}$ is considered as apparent diffusion coefficient. EIS was conducted with an amplitude of 5 mV over the frequency range of 100 kHz–10 mHz using a sinusoidal voltage by ZIVELAB potentiostat. The GITT was measured after formation cycles, where a current pulse of 0.2 A g⁻¹ was applied at voltage range 0.005–1.0 V for 10 min. Subsequently, a 6 h rest period was introduced to capture the response of electrode during relaxation. In GITT, chemical diffusion coefficient of Li⁺ ion was calculated based on following equation:

$$D_{\text{GITT}} = \frac{4}{\pi\tau} \left(\frac{m_B V_M}{M_B S} \right)^2 \left(\frac{\Delta E_S}{\Delta E_t} \right)^2 \quad (5)$$

where D_{GITT} , τ , M_B , and V_M are chemical diffusion coefficient of Li⁺, pulse time, and molar mass of active material and molar volume of active material. m_B , S , ΔE_S , and ΔE_t represent mass of the electrode material, area of the electrode–electrolyte interface, change of the steady state voltage, and total change of voltage during a pulse. Synchrotron-based *operando* analysis for *in situ* XRD variations on the full cell was performed using 9 A U-SAXS beamline of PLS-II with a wavelength of 0.6202 Å, where the XRD data were periodically collected with an interval of ≈3 min with a 2D CCD detector (SX165, Rayonix) in transmission mode.

Acknowledgements

This research was supported by the National Research Foundation of Korea (NRF) grant funded by the Korea government (MSIT) (RS-2024-00355916), by the National Research Foundation of Korea (NRF) grant funded by the Korea government (MSIT) (No. 2021R1A5A1084921), and by Korea Institute for Advancement of Technology (KIAT) grant funded by the Korea Government (MOTIE) (RS-2024-00419413, HRD Program for Industrial Innovation), and also by LG Energy Solution.

Conflict of Interest

The authors declare no conflict of interest.

Author Contributions

Junhyuk Ji: conceptualization (lead); data curation (lead); formal analysis (lead); investigation (lead); methodology (lead); validation (lead); visualization (lead); writing—original draft (lead). **Junchae Jeong:** formal analysis (supporting); validation (supporting). **Seochan Hong:** formal analysis (supporting); investigation (supporting). **Yongju Lee:** conceptualization (supporting); formal analysis (supporting); methodology (supporting); validation (supporting). **Donghyuk Kim:** formal analysis (supporting); investigation (supporting); methodology (supporting); validation (supporting). **Won Bae Kim:** conceptualization (lead); formal analysis (lead); funding acquisition (lead); methodology (lead); project administration (lead); supervision (lead); validation (lead); writing—review and editing (lead).

Data Availability Statement

The data that support the findings of this study are available from the corresponding author upon reasonable request.

Keywords: hydrogen • lithium-ion battery • microparticles • N-doped hard carbon • silicon

- [1] J. Xie, Y.-C. Lu, *Nat. Commun.* **2020**, *11*, 2499.
- [2] S. Jo, S. Seo, S. K. Kang, I. Na, S. Kunze, M. Song, S. Hwang, S. P. Woo, S. Kim, W. B. Kim, J. Lim, *Adv. Mater.* **2024**, *36*, 2402024.
- [3] M. Li, J. Lu, Z. Chen, K. Amine, *Adv. Mater.* **2018**, *30*, 1800561.
- [4] G. Zhu, D. Chao, W. Xu, M. Wu, H. Zhang, *ACS Nano* **2021**, *15*, 15567.
- [5] Y. An, X. Han, Y. Liu, A. Azhar, J. Na, A. K. Nanjundan, S. Wang, J. Yu, Y. Yamauchi, *Small* **2022**, *18*, 2103617.
- [6] Y. Katsuyama, Y. Li, S. Uemura, Z. Yang, M. Anderson, C. Wang, C.-W. Lin, Y. Li, R. B. Kaner, *ACS Appl. Mater. Interfaces* **2024**, *16*, 12612.
- [7] M. Je, M. Ham, S. Kim, Y. Park, S. Park, H. Lee, *ACS Appl. Mater. Interfaces* **2023**, *15*, 51215.
- [8] M. T. McDowell, S. W. Lee, W. D. Nix, Y. Cui, *Adv. Mater.* **2013**, *25*, 4966.
- [9] I. Byrd, J. Wu, *Electrochim. Acta* **2016**, *213*, 46.
- [10] J. Chang, X. Huang, G. Zhou, S. Cui, S. Mao, J. Chen, *Nano Energy* **2015**, *15*, 679.
- [11] G. Sikha, S. De, J. Gordon, *J. Power Sources* **2014**, *262*, 514.
- [12] J. Li, N. J. Dudney, X. Xiao, Y. Cheng, C. Liang, M. W. Verbrugge, *Adv. Energy Mater.* **2015**, *5*, 1401627.
- [13] A. Toudjine, M. Morcrette, M. Courty, C. Davoisne, M. Lejeune, N. Mariage, W. Porcher, D. Larcher, *J. Electrochem. Soc.* **2015**, *162*, A1466.
- [14] K. A. Hays, B. Key, J. Li, D. L. Wood, G. M. Veith, *J. Phys. Chem. C* **2018**, *122*, 9746.
- [15] L. Sun, Y. Liu, L. Wang, Z. Jin, *Adv. Funct. Mater.* **2024**, *34*, 2403032.
- [16] J. Park, S. K. Kang, J. Ji, H. Ahn, G. H. Park, M. Kim, W. B. Kim, *J. Energy Chem.* **2024**, *98*, 134.
- [17] G. Song, M. J. Kwak, C. Hwang, C. An, S. Kim, S. Lee, S. Choi, H. K. Song, J. H. Jang, S. Park, *ACS Appl. Energy Mater.* **2021**, *4*, 10050.
- [18] M. Je, H. B. Son, Y. Han, H. Jang, S. Kim, D. Kim, J. Kang, J. Jeong, C. Hwang, G. Song, H. Song, T. S. Ha, S. Park, *Adv. Sci.* **2024**, *11*, 2305298.
- [19] S. Chae, S. Choi, N. Kim, J. Sung, J. Cho, *Angew. Chem., Int. Ed.* **2020**, *59*, 110.
- [20] I. Ryu, S. W. Lee, H. Gao, Y. Cui, W. D. Nix, *J. Power Sources* **2014**, *255*, 274.
- [21] Z. Wang, Z. Mao, L. Lai, M. Okubo, Y. Song, Y. Zhou, X. Liu, W. Huang, *Chem. Eng. J.* **2017**, *313*, 187.
- [22] J. Lopez, Z. Chen, C. Wang, S. C. Andrews, Y. Cui, Z. Bao, *ACS Appl. Mater. Interfaces* **2016**, *8*, 2318.
- [23] C. Li, W. Zhu, B. Lao, X. Huang, H. Yin, Z. Yang, H. Wang, D. Chen, Y. Xu, *ChemElectroChem* **2020**, *7*, 3743.
- [24] R. Nandan, N. Takamori, K. Higashimine, R. Badam, N. Matsumi, *J. Mater. Chem. A* **2022**, *10*, 15960.

- [25] K. G. Araño, G. Yang, B. L. Armstrong, T. Aytug, M. S. Chambers, E. C. Self, H. M. Meyer, J. Quinn, J. F. Browning, C. Wang, G. M. Veith, *ACS Appl. Energy Mater.* **2023**, *6*, 11308.
- [26] J. Han, C. Zhao, L. Wang, J. Song, D. Yang, Q. Tian, *J. Alloys Compd.* **2023**, *966*, 171668.
- [27] L. Zhang, Y. Liu, B. Key, S. E. Trask, Z. Yang, W. Lu, *ACS Appl. Mater. Interfaces* **2017**, *9*, 32727.
- [28] C.-L. Zhang, H. Li, Q. Zhang, F.-H. Cao, Y. Xie, B.-R. Lu, W.-D. Zhang, H.-P. Cong, H. Li, *Chem. Eng. J.* **2021**, *420*, 127705.
- [29] D. Wang, Q. Wang, Z. Lin, T. Pang, N. Ding, *Crystals* **2023**, *13*, 607.
- [30] J. Prakash, K. Dasgupta, B. M. Tripathi, J. Bahadur, S. K. Ghosh, J. K. Chakravarthy, *J. Mater. Sci.* **2014**, *49*, 6784.
- [31] E. Härik, M. Ballauff, *C* **2020**, *6*, 82.
- [32] L. Liu, Y. Tian, A. Abdussalam, M. R. H. S. Gilani, W. Zhang, G. Xu, *Molecules* **2022**, *27*, 6516.
- [33] F. Wang, S. Lin, X. Lu, R. Hong, H. Liu, *Electrochim. Acta* **2022**, *404*, 139708.
- [34] R. Cong, M. Jo, A. Martino, H.-H. Park, H. Lee, C.-S. Lee, *Sci. Rep.* **2022**, *12*, 16002.
- [35] A. Agrawal, K. Biswas, S. K. Srivastava, S. Ghosh, *J. Solid State Electrochem.* **2018**, *22*, 3443.
- [36] S. Lee, W. Yoon, J. Ji, H. Ahn, W. B. Kim, *J. Environ. Chem. Eng.* **2022**, *10*, 108325.
- [37] S. G. Jung, M. S. Rani, J. Bae, S. K. Kang, G. H. Park, J. Ji, W. B. Kim, *Korean J. Chem. Eng.* **2024**, *41*, 2029.
- [38] J. Bae, J. Ji, M. Kim, S. K. Kang, G. H. Park, Y. H. Jeong, C. Jo, W. B. Kim, *Energy Fuels* **2023**, *37*, 12445.
- [39] L. Sun, Y. Liu, J. Wu, R. Shao, R. Jiang, Z. Tie, Z. Jin, *Small* **2022**, *18*, 2102894.
- [40] Z. Li, Y. Zhang, T. Liu, X. Gao, S. Li, M. Ling, C. Liang, J. Zheng, Z. Lin, *Adv. Energy Mater.* **2020**, *10*, 1903110.
- [41] C. Qi, S. Li, Z. Yang, Z. Xiao, L. Zhao, F. Yang, G. Ning, X. Ma, C. Wang, J. Xu, J. Gao, *Carbon* **2022**, *186*, 530.
- [42] B. Li, H. Hu, H. Hu, C. Huang, D. Kong, Y. Li, Q. Xue, Z. Yan, W. Xing, X. Gao, *Electrochim. Acta* **2021**, *370*, 137717.
- [43] Y. Ko, C. Hwang, H.-K. Song, *J. Power Sources* **2016**, *315*, 145.
- [44] Y. Yu, C. Yang, Y. Jiang, J. Zhu, Y. Zhao, S. Liang, K. Wang, Y. Zhou, Y. Liu, J. Zhang, M. Jiang, *Small* **2023**, *19*, 2303779.
- [45] K. Ando, T. Matsuda, D. Imamura, *J. Energy Chem.* **2021**, *53*, 285.
- [46] S. K. Kang, M. Kim, G. H. Park, J. Ji, S. Hong, W. B. Kim, *Adv. Funct. Mater.* **2025**, *35*, 2408986.
- [47] Z. Li, Z. Zhao, S. Pan, Y. Wang, S. Chi, X. Yi, J. Han, D. Kong, J. Xiao, W. Wei, S. Wu, Q. Yang, *Adv. Energy Mater.* **2023**, *13*, 2300874.
- [48] Y. Zhang, C. Yin, B. Qiu, G. Chen, Y. Shang, Z. Liu, *Energy Storage Mater.* **2022**, *53*, 763.
- [49] A. Nulu, Y. G. Hwang, V. Nulu, K. Y. Sohn, *Nanomaterials* **2022**, *12*, 3004.
- [50] X. Li, M. Zhang, S. Yuan, C. Lu, *ChemElectroChem* **2020**, *7*, 4289.
- [51] T. Kim, W. Choi, H.-C. Shin, J.-Y. Choi, J. M. Kim, M.-S. Park, W.-S. Yoon, *J. Electrochem. Sci. Technol.* **2020**, *11*, 14.
- [52] S.-B. Kim, H. Kim, D.-H. Park, J.-H. Kim, J.-H. Shin, J.-S. Jang, S.-H. Moon, J.-H. Choi, K.-W. Park, *J. Power Sources* **2021**, *506*, 230219.
- [53] K. Tang, X. Yu, J. Sun, H. Li, X. Huang, *Electrochim. Acta* **2011**, *56*, 4869.
- [54] Y. Jiang, J. Liu, *Energy Environ. Mater.* **2019**, *2*, 30.
- [55] J. Wu, X. Zhang, Z. Li, C. Yang, W. Zhong, W. Li, C. Zhang, N. Yang, Q. Zhang, X. Li, *Adv. Funct. Mater.* **2020**, *30*, 2004348.
- [56] J. Wang, J. Polleux, J. Lim, B. Dunn, *J. Phys. Chem. C* **2007**, *111*, 14925.
- [57] M. Kim, S. K. Kang, J. Choi, H. Ahn, J. Ji, S. H. Lee, W. B. Kim, *Nano Lett.* **2022**, *22*, 10232.
- [58] J. Ji, M. Park, M. Kim, S. K. Kang, G. H. Park, J. Maeng, J. Ha, M. H. Seo, W. B. Kim, *Adv. Sci.* **2024**, *11*, 2402389.
- [59] S. Yi, Z. Yan, X. Li, Z. Wang, P. Ning, J. Zhang, J. Huang, D. Yang, N. Du, *Chem. Eng. J.* **2023**, *473*, 145161.
- [60] L. Li, C. Fang, G. He, Y. Huang, *ACS Appl. Mater. Interfaces* **2023**, *15*, 2310240.
- [61] Y. Wei, Z. Xiao, Y. Huang, Y. Zhu, Z. Zhu, Q. Zhang, D. Jia, S. Zhang, F. Wei, *Small* **2024**, *20*, 1.
- [62] L. Lv, Y. Wang, W. Huang, Y. Li, Q. Shi, H. Zheng, *ACS Appl. Mater. Interfaces* **2022**, *14*, 35246.
- [63] P. Shi, Z.-Y. Liu, X.-Q. Zhang, X. Chen, N. Yao, J. Xie, C.-B. Jin, Y.-X. Zhan, G. Ye, J.-Q. Huang, *J. Energy Chem.* **2022**, *64*, 172.
- [64] Y. Wang, H. Xu, X. Chen, H. Jin, J. Wang, *Energy Storage Mater.* **2021**, *38*, 121.
- [65] S. Pan, J. Han, Y. Wang, Z. Li, F. Chen, Y. Guo, Z. Han, K. Xiao, Z. Yu, M. Yu, S. Wu, D. Wang, Q. Yang, *Adv. Mater.* **2022**, *34*, 2203617.
- [66] X. Yang, X. Chen, J. Qiu, M. Li, H. Ming, S. Zhang, T. Zhang, *J. Solid State Chem.* **2021**, *296*, 121968.
- [67] X. Li, M. Tabish, W. Zhu, X. Chen, H. Song, *Small* **2023**, *19*, 2302388.
- [68] L. Fu, A. Xu, Y. Song, J. Ju, H. Sun, Y. Yan, S. Wu, *Electrochim. Acta* **2021**, *387*, 138461.
- [69] Q. Huang, J. Song, Y. Gao, D. Wang, S. Liu, S. Peng, C. Usher, A. Goliaszewski, D. Wang, *Nat. Commun.* **2019**, *10*, 5586.
- [70] Z. Xu, E. Zheng, Z. Xiao, H. Shao, Y. Liu, J. Wang, *Chem. Eng. J.* **2023**, *459*, 141543.
- [71] X. Zhang, R. Guo, X. Li, L. Zhi, *Small* **2018**, *14*, 1800752.
- [72] C.-H. Jung, K.-H. Kim, S.-H. Hong, *J. Mater. Chem. A* **2019**, *7*, 12763.
- [73] M. Li, J. Qiu, S. Zhang, P. Zhao, Z. Jin, A. Wang, Y. Wang, Y. Yang, H. Ming, *J. Energy Chem.* **2020**, *50*, 286.
- [74] T. Zhou, X. Yu, F. Li, J. Zhang, B. Liu, L. Wang, Y. Yang, Z. Hu, J. Ma, C. Li, G. Cui, *Energy Storage Mater.* **2023**, *55*, 691.
- [75] Z. Dai, J. Wang, H. Zhao, Y. Bai, *Adv. Sci.* **2022**, *9*, 2200622.
- [76] H. Ahn, J. Choi, M. Kim, S. K. Kang, D. Jang, J. Maeng, G. H. Park, J. Ji, J. Ha, W. B. Kim, *Chem. Mater.* **2024**, *36*, 4379.
- [77] K. Du, A. Gao, L. Gao, S. Sun, X. Lu, C. Yu, S. Li, H. Zhao, Y. Bai, *Nano Energy* **2021**, *83*, 105775.

Manuscript received: January 31, 2025

Revised manuscript received: April 21, 2025

Version of record online: May 6, 2025